An Integrated Three-Port Bidirectional DC–DC Converter for PV Application on a DC Distribution System

Zhan Wang, *Student Member, IEEE*, and Hui Li, *Senior Member, IEEE*

***Abstract*—In this paper, an integrated three-port bidirectional dc–dc converter for a dc distribution system is presented. One port of the low-voltage side of the proposed converter is chosen as a current source port which fits for photovoltaic (PV) panels with wide voltage variation. In addition, the interleaved structure of the current source port can provide the desired small current ripple to benefit the PV panel to achieve the maximum power point tracking (MPPT). Another port of the low-voltage side is chosen as a voltage source port interfaced with battery that has small voltage variation; therefore, the PV panel and energy storage element can be integrated by using one converter topology. The voltage port on the high-voltage side will be connected to the dc distribution bus. A high-frequency transformer of the proposed converter not only provides galvanic isolation between energy sources and high voltage dc bus, but also helps to remove the leakage current resulted from PV panels. The MPPT and power flow regulations are realized by duty cycle control and phase-shift angle control, respectively. Different from the single-phase dual-half-bridge converter, the power flow between the low-voltage side and high-voltage side is only related to the phase-shift angle in a large operation area. The system operation modes under different conditions are analyzed and the zero-voltage switching can be guaranteed in the PV application even when the dc-link voltage varies. Finally, system simulation and experimental results on a 3-kW hardware prototype are presented to verify the proposed technology.**

***Index Terms*—Bidirectional, dc–dc converters, dc distribution, multiport, photovoltaic (PV) system, zero-voltage switching (ZVS).**

NOMENCLATURE

DES	Distribution energy system.
ICE	Internal combustion engines.
DHB	Dual half-bridge.
DAB	Dual active bridge.
DAB3	Three-phase dual active bridge.
LVS	Low-voltage side.
HVS	High-voltage side.
ZVS	Zero-voltage switching.
BU	Battery unit.
SOC	State of charge.
L_s	Leakage inductance.
D	Duty cycle.
f	Switching frequency.
φ	Phase-shift angle.
d	Ratio of dc-link voltage of secondary side and primary side.
m	Ratio of dc inductance and transformer leakage inductance.
n	Ratio of PV power to per unit power.

Manuscript received July 25, 2012; revised October 6, 2012 and December 12, 2012; accepted December 13, 2012. Date of current version March 15, 2013. This work was supported by the National Science Foundation under Award ECCS-0641972. Recommended for publication by Associate Editor J. A. Pomilio.

Z. Wang is with ABB Corporate Research Center, Raleigh, NC 27606 USA (e-mail: zhan.wang@us.abb.com).

H. Li is with the Department of Electrical and Computer Engineering, Florida State University, Tallahassee, FL 32310 USA (e-mail: hli@caps.fsu.edu).

Color versions of one or more of the figures in this paper are available online at http://ieeexplore.ieee.org.

Digital Object Identifier 10.1109/TPEL.2012.2236580

I. INTRODUCTION

DC DESs have the advantages to interact with renewable energy source due to the simplicity and efficiency [1]. Distributed energy resources include but are not limited to photovoltaic (PV) and fuel cell, which generate dc voltage; as well as wind turbine, microturbine, and internal combustion engines, which generate ac voltage. All of these resources have to be interfaced with a dc bus and feed power to the load or the utility grid; therefore, dc–dc or ac–dc power electronics converters are essential units [2]–[8]. Moreover, the energy storage system can balance the difference between the renewable energy source and the load requirement. It also helps intensive penetration of renewable energy production such as PV into the grid by providing peak shaving service at the lowest cost [1], [9]–[11]. Power electronics converters are also required to interface energy storage elements to the grid or the load. A common dc distribution bus shared by these converters is an effective solution, since the total number of converters is lower compared with the ac solution, even if it is necessary to have an ac–dc interface converter with the utility grid [8].

DC–DC converters are essential in dc distribution systems since they connect not only dc sources but dc energy storage to the dc distribution bus. This paper is focused on developing a novel dc–dc converter for distributed PV applications on a dc distribution system, which is shown in Fig. 1.

In this system, a basic cell of the DES consists of an energy source, i.e., PV panels in this paper, and an energy storage element such as batteries. A multiport dc–dc converter as an attractive solution is suitable to integrate the PV and energy storage element with the advantages of high efficiency, high power density, and cost effective, which has been addressed in various literatures [12]–[19]. In [12] and [13], a three-port converter has been proposed to interface with PV and

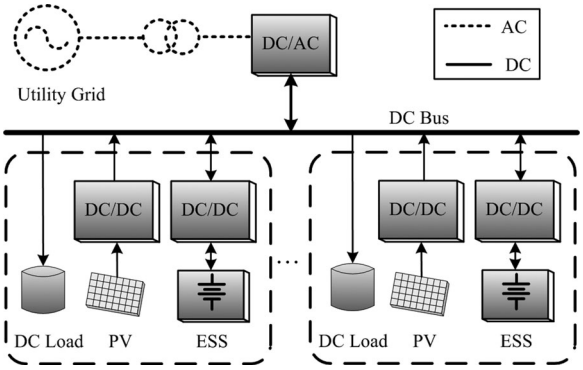

Fig. 1. DC distribution system with a basic cell for PV applications: energy sources, energy storage element, and load.

batteries. However, the presented converter is not able to charge the battery from the common dc-bus side due to the unidirectional power flow between the primary side and secondary side. Moreover, the power control of PV and battery is coupled so that a decoupled controller should be designed. Another popular topology is the three-port transformer-coupled DAB converter for renewable energy system application, which has been addressed in [14]–[18]. Since it is magnetic coupled, all of three-port are galvanic isolated and the bidirectional power flow is guaranteed. In this topology, however, since only one multiwinding transformer is applied to interface with three half or full bridges, there exists circulating current in the three-port dc–dc converter. Therefore, how to minimize the circulation power loss needs to be considered for this type of topology, which has been pointed out by the authors in [17] and [19]. An interleaved triple-voltage dc–dc converter has been discussed in [20], which consists of two half-bridges and a high-frequency transformer to provide voltage level matching and galvanic isolation. The interleaved structure is to reduce the capacitor requirement and current ripple. Since the dc inductor is removed and the low-voltage source directly connects to the midpoint of the split capacitors, there is large current ripple in the low-voltage source, which is not good for ripple sensitive power sources such as PV. A low-cost, soft-switched bidirectional dc–dc converter for connecting the three voltage nets is discussed in [21]. Based on this topology, an interleaved reduced-component-count three-voltage bus dc–dc converter is proposed for fuel cell electric vehicle applications to reduce the capacitor requirements and current ripple [22]. The dc inductor is not required in this topology, but it is not easy to realize the power flow management between two low-voltage ports. Since the voltage is fixed in these applications [20]–[22], the duty cycle is set to around 1/3 and the varied duty cycle control is not analyzed; the power flow between two low-voltage ports has not been studied either. In addition, it can be expected that when the duty cycle control is applied, the soft-switching conditions and controller will be affected, which needs to be investigated.

In this paper, a three-port bidirectional dc–dc converter for a PV system applied on dc distribution is proposed. One port of the LVS of the proposed converter is designed as a current source port that PV panels are connected to meet the maximum power point tracking (MPPT) and voltage variation requirement. The battery pack is connected to the LVS dc-link due to its small voltage variation. The dc distributed bus is connected to the HVS port to realize galvanic isolation by a high-frequency transformer. The advantages of proposed converter have been summarized as follows. First, compared to the single-phase DHB converters, the three-phase interleaved structure reduces passive components size, current, and voltage ripples. The interleaved structure reduces the total input current ripple by using a small value of dc inductors, and at the same time, a large current ripple in each dc inductor can help to improve the soft-switching condition further. Benefited from the dc current ripple, a ZVS can be guaranteed in different operation modes even when the PV voltage varies in a wide voltage range and the battery voltage changes in a small voltage range with different SOCs and charge/discharge status. In addition, compared to other two-phase converters (DAB) or other n-phase ($n > 3$) converters, the power flow control of the proposed three-port converter is naturally decoupled in a wide operation range; therefore, it can be treated as a boost-stage converter cascaded with a three-phase DAB-stage converter. Since in the main operation range, the power flow is just related to the phase-shift angle no matter what the duty cycle is, the succinct power equation of the three-phase converter is helpful for the derivation of the mathematical model and control system design. For other n-phase ($n > 3$) converters, the fundamental model analysis has to be applied due to the complex piecewise power equations [17], [23]. However, it should be noticed that when the duty cycle changes, the accuracy of the fundamental model will be lost. Therefore, only the three-phase topology does not increase the complexity of the system; however, on the contrary, the controller can be designed separately where the control of the boost stage is to achieve MPPT and voltage step-up functions; the control of the DAB stage is to meet the requirements of the battery operation and dc distribution bus connection.

II. Converter Description

Fig. 2 shows the proposed integrated three-port dc–dc converter topology. A three-phase DAB converter is applied to realize the bidirectional power flow function and the Y-Y connected high-frequency transformers can provide galvanic isolation and voltage-level matching between low-voltage energy sources and high-voltage dc bus. The leakage inductances $L_{s1} - L_{s3}$ of the transformer are used as energy storage elements to transfer the power between two sides, and the power flow is mainly controlled by a phase-shift angle φ. The middle points of three legs in the LVS are connected to one energy source port through three dc inductors $L_{\mathrm{dc1}} - L_{\mathrm{dc3}}$, and duty cycle D is another control variable to adjust the power distribution between the two ports of the LVS. In the application of a PV system on dc distribution bus, the converter is applied to interface with PV panels, BU, and dc bus or load. The BU is connected to the LVS dc link. The voltage of the battery changes slowly with different SOCs, so the primary-side dc-link voltage can be treated as almost constant. The PV panels are connected to the current source

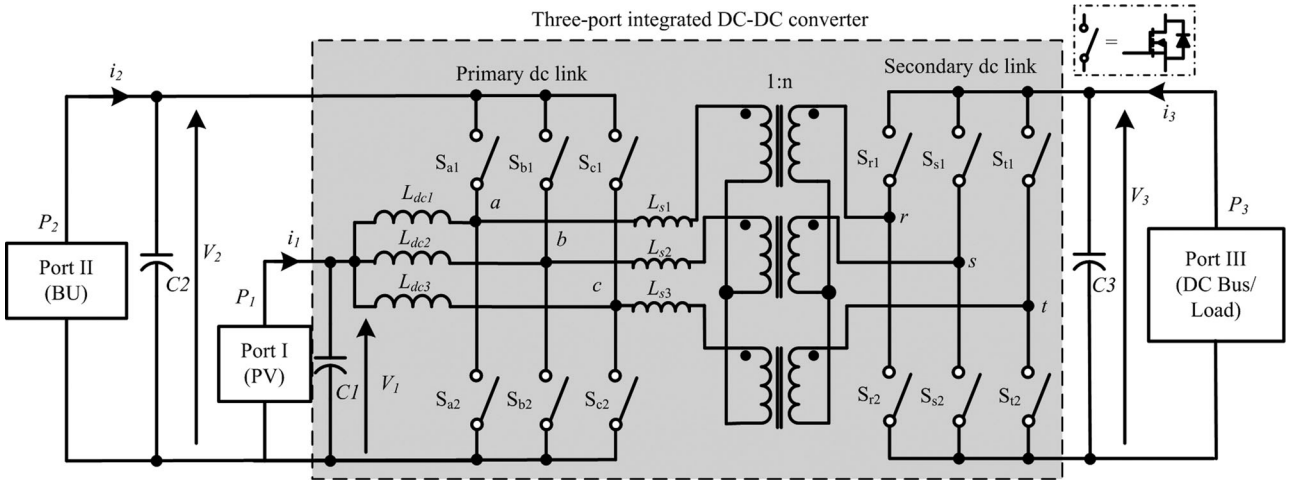

Fig. 2. Proposed three-port integrated bidirectional dc–dc converter.

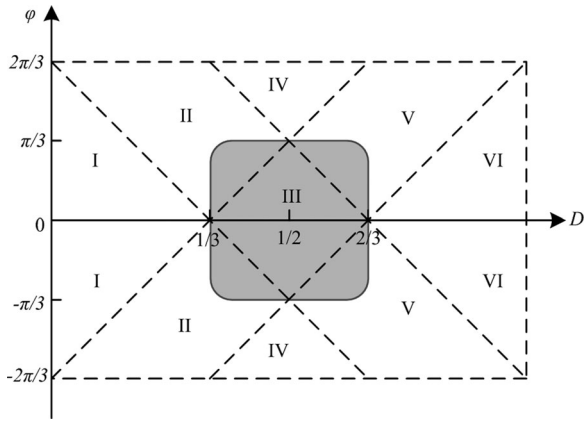

Fig. 3. Six operation areas with different duty cycle and phase-shift angle; the shadowed part is the practical operating area.

port. The output voltage and current of PV change in a large range due to different solar irradiation and ambient temperature. Three-phase dc inductors and primary-side switches are used to boost the PV voltage and MPPT can be realized by the duty cycle control. With the help of dc inductors, the ZVS is guaranteed in all the operation modes, even though the battery's voltage changes with different SOCs. Compared to the single-phase topology, the three-phase interleaved topology can reduce the current and voltage ripples to reduce the inductor and capacitor's size.

The modulation strategy of the three port is similar to that of a two-port DAB3 converter, so the converter operation range is similar to that of the DAB3 converter [23] and is shown in Fig. 3. It can be seen that the converter operation range is divided into six areas; and the power flow between the LVS and HVS will change according to different combinations of duty cycle and phase-shift angle. In real applications, in order to operate the converter to achieve high efficiency, the duty cycle is limited between 1/3 and 2/3, and the phase-shift angle should be smaller than $\pi/3$ for low reactive power loss. For example, when the converter is mainly operating in Area III, the power

TABLE I
OPERATION MODES IN TERMS OF DIFFERENT POWER FLOWS

		$P_{PV} > 0$	$P_{PV} = 0$
$P_{Bus} < 0$	$P_{Bat} < 0$	Mode A	Doesn't exist
	$P_{Bat} > 0$	Mode B	Mode D
$P_{Bus} > 0$	$P_{Bat} < 0$	Mode C	Mode E
	$P_{Bat} > 0$	Doesn't exist	Doesn't exist

equation is given in [23]

$$P_{\mathrm{III}} = \frac{V_2 V_3'}{\omega L_s} \frac{\varphi(4\pi - 3|\varphi|)}{6\pi} \tag{1}$$

where V_2 is the LVS dc-link voltage, V_3' is the HVS bus voltage referred to the LVS, and $V_3' = V_3/n$. The phase-shift angle φ can be calculated as

$$|\varphi| = \frac{2\pi}{3}\left(1 - \sqrt{1 - \frac{3|P_{\mathrm{III}}| f L_s}{V_2 V_3'}}\right). \tag{2}$$

Although the operation range and the power transferred from the LVS to the HVS of the proposed three-port converter is similar to those of the two-port DAB3 converter, the operation modes of the three-port converter are quite different due to extra power flow combinations of the three-port converter, which are listed in Table I. Since the PV panels cannot sink power, there are five operation modes. Fig. 4 shows the operation modes with different power flows where P_1, P_2, and P_3 represent the power from the corresponding three ports, and the positive power means that the power is generated from the port. Due to the power conservation law, the power satisfies

$$P_1 + P_2 + P_3 = 0. \tag{3}$$

In Mode A, when $P_1 = -P_2 - P_3 > 0$, the solar irradiation is high, PV can provide power to the dc bus, and charge the battery at the same time. In this mode, the BU functions to store the extra energy. The objective of power control in Mode A can be either the battery's charging current I_{bat} or the scheduled dc bus current I_{bus}. If I_{bus} is chosen as the control objective, the relationship of φ in terms of I_{bus} can be derived in (4.1). If I_{bat}

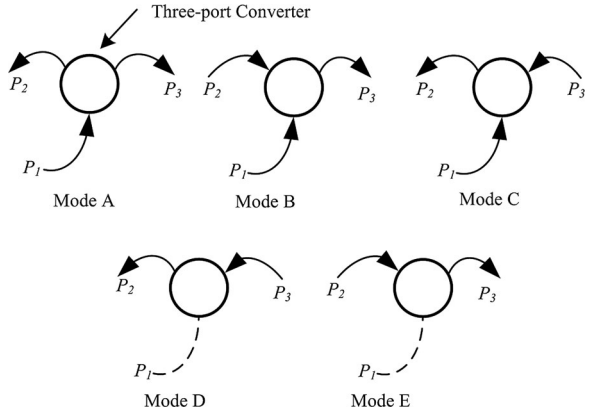

Fig. 4. Operation modes with different power flows. Mode A: $P_1 > 0$, $P_2 < 0$, $P_3 < 0$; Mode B: $P_1 > 0$, $P_2 > 0$, $P_3 < 0$; Mode C: $P_1 > 0$, $P_2 < 0$, $P_3 > 0$; Mode D: $P_1 = 0$, $P_2 < 0$, $P_3 > 0$; Mode E: $P_1 = 0$, $P_2 > 0$, $P_3 < 0$.

is the control target, φ in terms of $I_{\rm bat}$ is derived as follows:

$$\varphi = \frac{2\pi}{3}\left(1 - \sqrt{1 - \frac{3nfL_sI_{\rm bus}}{V_2}}\right) \tag{4.1}$$

$$\varphi = \frac{2\pi}{3}\left(1 - \sqrt{1 - \frac{3nfL_s\left(P_1 - V_2I_{\rm bat}\right)}{V_3V_2}}\right). \tag{4.2}$$

In Mode B, when $P_1+P_2 = -P_3 > 0$, the solar power is not high enough, so PV with BU together will provide power to meet the scheduled dc-bus load requirement and the BU functions as an energy source to support the dc-bus load. In this mode, only the bus current $I_{\rm bus}$ can be controlled; therefore, φ is derived in (5) in terms of $I_{\rm bus}$

$$\varphi = \frac{2\pi}{3}\left(1 - \sqrt{1 - 3nfL_sI_{\rm bus}/V_2}\right). \tag{5}$$

In Mode C, when $P_1+P_3 = -P_2 > 0$, the SOC of the battery is low, and the PV and dc bus will provide power to charge the battery. Since the constant charging current is preferred, the dc-bus power is used to make it constant and mitigate the disturbance resulted from the PV power. The relationship between φ and $I_{\rm bat}$, the control target, is illustrated as follows:

$$\varphi = -\frac{2\pi}{3}\left(1 - \sqrt{1 - 3fL_sI_{\rm bat}/V_3'}\right). \tag{6}$$

In Mode D, when $P_3 = -P_2 > 0$, there is no solar power in the evening or cloudy days, and the power from the dc bus can charge the battery. This mode is used to save the grid energy into the energy storage system when the utility price is low at night or there is excessive power generated from other energy source. The control objective is $I_{\rm bat}$ and the following equation shows how φ is depending on $I_{\rm bat}$ in Mode D:

$$\varphi = -\frac{2\pi}{3}\left(1 - \sqrt{1 - 3fL_sI_{\rm bat}/V_3'}\right). \tag{7}$$

In Mode E, when $P_2 = -P_3 > 0$, there is no PV power, and the battery can discharge to meet the requirement of dc-bus load. This mode mainly happens in the standalone mode and there is no other energy source available to support the load. The BU functions as a backup energy source to provide uninterruptable power. Since $I_{\rm bat}$ is the control objective in this mode, the relationship between φ and $I_{\rm bat}$ is derived as follows:

$$\varphi = -\frac{2\pi}{3}\left(1 - \sqrt{1 - 3fL_sI_{\rm bat}/V_3'}\right). \tag{8}$$

Equations (4)–(8) provide the insight information between the control objective ($I_{\rm bat}$ or $I_{\rm bus}$) and control variable φ in Modes A–E, which will help to design the controller in these modes. There are other operation modes in which the solar power is only used to charge the battery or the solar power is only used to support the dc-bus load, but they are not common and can be avoided with a proper power management strategy. In addition, the optimized power management strategy is out of scope here, so the mode sequence optimization will not be discussed in this paper.

III. ZVS and Conduction Loss Analysis

A. ZVS Condition Derivation

The soft-switching condition of the three-port topology is different from that of the two-port converter in [23]. This is because the power generated or sunk from the energy storage element will have an influence on the switches' current on the primary side. Hence, the ZVS analysis is essential and analyzed in this section.

The soft-switching conditions of the DAB3 converter will be guaranteed when the dc-link voltages on both sides are matched [23]. For the three-port dc–dc converter applied for PV systems on a dc distribution bus, the ZVS conditions should be derived separately in different operation modes. The ZVS conditions will be also affected by the voltage variation due to the battery's voltage changes with the SOC. Fig. 5 shows the circuits of one leg on the LVS, as well as the denotation of current in each branch. The current flow through the MOSFETs will be affected by the transformer current together with the dc inductor current. When the upper switch is gated ON, the current flowing through it is equal to $i_s - i_{\rm dc}$. If i_{a1_on} is negative, S_{a1} is turned ON at zero voltage. When the lower switch is gated ON, the current flowing through it is equal to $i_{\rm dc} - i_s$. If i_{a2_on} is negative, S_{a2} is turned ON at zero voltage. It can be noticed from Fig. 5 that the positive average dc inductor current is helpful for S_{a1} ZVS achievement but harmful for S_{a2}, and the dc inductor current ripple can help us to improve the ZVS conditions for both switches. The inductor current and transformer current waveforms will vary in different operation modes. Therefore, the soft-switching conditions have to be analyzed according to the different scenario.

1) Pseudo "Two-Port" ZVS Analysis: When PV does not provide power, it becomes a two-port condition. However, this two-port soft switching is different from the two-port soft switching in [24], because in [24], the power in the primary side is generated from the current source port and in this paper, the power is provided from the battery which is connected to the primary-side dc link. It is also different from the DAB3 converter in [23] because there is a dc inductor current in the primary side that will change the current waveform in switches,

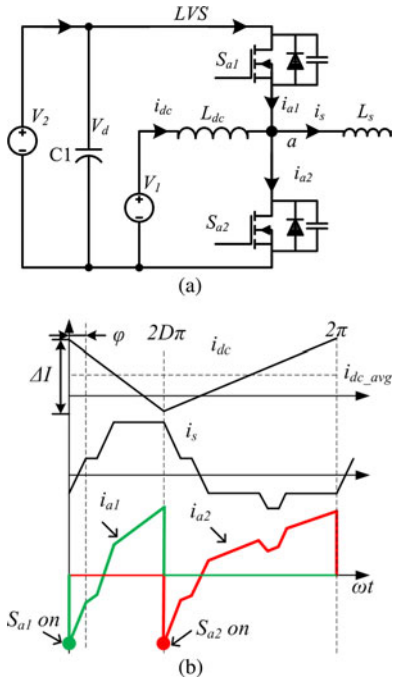

Fig. 5. Circuit of one leg on the LVS and the corresponding current in one switching cycle.

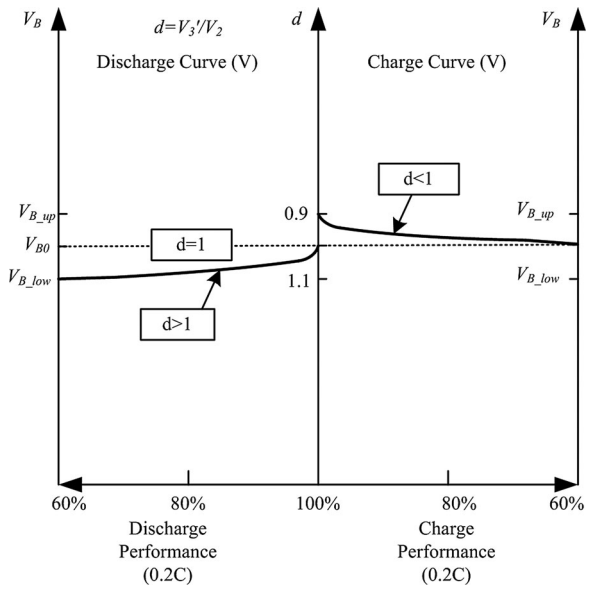

Fig. 6. Battery's voltage in charge/discharge performance.

thus affecting the ZVS conditions. Therefore, it is defined as the pseudo "two-port" ZVS condition in this paper.

In our application, the voltage variation in the battery due to the SOC should also be considered. When the primary-side dc-link voltage changes with the SOC of the battery, $d = V_3'/V_2$ will change around 1, which is shown in Fig. 6. During discharging, the battery's voltage will decrease and d is higher than "1." During charging, the battery's voltage will increase and d is lower than "1." However, with the help of dc inductor current ripples, the ZVS can be guaranteed when d is changing between 0.9 and 1.1.

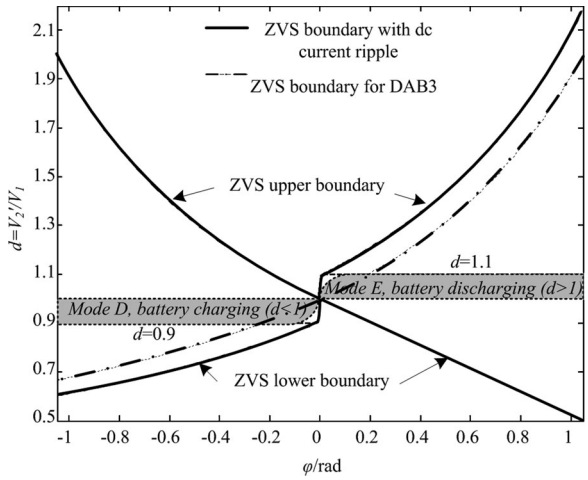

Fig. 7. ZVS in the pseudo "two-port" condition including Modes D and E.

Let $m = L_{\rm dc}/L_s$; the dc inductor current ripple of each phase can be calculated as

$$\Delta I_{\rm dc} = \frac{2D(1-D)\pi}{m\omega L_s} V_d. \tag{9}$$

The ZVS conditions of the switches for one phase should satisfy the following equation:

$$\begin{cases} Sa1: \dfrac{1}{2}\Delta I_{\rm dc} - i_{Ls}\left(t_{Sa1_{\rm on}}\right) > 0 \\ Sa2: \dfrac{1}{2}\Delta I_{\rm dc} + i_{Ls}\left(t_{Sa2\_{\rm on}}\right) > 0 \\ Sr1: i_{Ls}\left(t_{Sr1\_{\rm on}}\right) > 0 \\ Sr2: i_{Ls}\left(t_{Sr2\_{\rm on}}\right) < 0. \end{cases} \tag{10}$$

According to (10), the constraint conditions of ZVS related to d can be derived. Because in different operation areas, the transformer current is different, the ZVS conditions should be calculated separately. In PV applications, the converter is mainly operating in the area of $(D,\varphi) \in \left(\left[\frac{1}{3},\frac{2}{3}\right],\left[-\frac{\pi}{3},\frac{\pi}{3}\right]\right)$, and the expressions of power and current can be calculated in corresponding operating Areas II, III, and V. The detailed calculation is shown in the Appendix. For instance, the range of d should satisfy the following equation to meet the ZVS conditions:

$$\begin{cases} \dfrac{2\pi-3\varphi}{2\pi} \le d \le \dfrac{2m+D(1-D)}{2\pi-3\varphi}\pi, & \varphi \ge 0 \\ \dfrac{2m-9D(1-D)}{2\pi-3\varphi}\pi \le d \le \dfrac{2\pi}{2\pi+3\varphi}, & \varphi \le 0. \end{cases} \tag{11}$$

In PV applications, the battery's voltage will vary with different SOCs and charge/discharge status. Fig. 7 shows the soft-switching conditions of the proposed three-port converter at pseudo "two-port" condition. The ZVS boundary in Fig. 7 is derived from (11). The converter is operating in the shadowed area. d is set as 0.9 in the charging mode and 1.1 in the discharging mode, which are two extreme cases and can be observed from Fig. 6. Fig. 7 shows that the operation curves are always located between the upper and lower ZVS boundaries so that soft switching can be guaranteed in the whole operating range at pseudo "two-port" condition. In addition, the pseudo "two-port"

condition includes operation Modes D and E; therefore, the soft-switching conditions of Modes D and E are guaranteed. Fig. 7 also shows that the soft switching at the worst case happens when φ is 0

$$1-\frac{9D(1-D)}{2m}\le d\le 1+\frac{9D(1-D)}{2m},\quad \varphi=0. \tag{12}$$

In the DAB3 converter, only "$d=1$" can meet the soft-switching condition at $\varphi=0$. However, compared to the DAB3 converter, the ZVS range of the proposed three-port converter is enlarged in the primary side.

2) "Three-Port" ZVS Analysis: In "three-port" conditions, the soft switching is not only related to dc inductor current but also to the PV power. Let the PV power be $P_{\rm PV}=n\frac{V_o'^2}{\omega L_s}$; then, the average PV current of each phase is

$$I_{\rm dc\_avg}=\frac{P_{\rm PV}}{3DdV_o'}=\frac{nV_o'}{3Dd\omega L_s}. \tag{13}$$

According to different power flow directions, (10) should be satisfied

$$\begin{cases} Sa1: I_{\rm dc\_avg}+\dfrac{1}{2}\Delta I_{\rm dc}-i_{Ls}\left(t_{Sa1_{\rm on}}\right)>0\\ Sa2: -I_{\rm dc_{avg}}+\dfrac{1}{2}\Delta I_{\rm dc}+i_{Ls}\left(t_{Sa2\_{\rm on}}\right)>0\\ Sr1: i_{Ls}\left(t_{Sr1\_{\rm on}}\right)>0\\ Sr2: i_{Ls}\left(t_{Sr2\_{\rm on}}\right)<0. \end{cases} \tag{14}$$

As discussed previously, the pseudo "two-port" ZVS analysis includes those of Modes D and E, and the "three-port" ZVS analysis will cover the ZVS conditions of the rest of modes. Equation (14) should be satisfied by these three modes. According to (14), the ZVS conditions of each switch in Area III can be calculated as

$$\begin{cases} Sa1: d<9\dfrac{\frac{n}{3D}+\frac{D(1-D)}{m}\pi+\frac{2}{9}\pi}{2\pi-3\varphi}\\ Sa2: d<9\dfrac{-\frac{n}{3D}+\frac{D(1-D)}{m}\pi+\frac{2}{9}\pi}{2\pi-3\varphi}\\ Sr1: d>\dfrac{2\pi-3\varphi}{2\pi}\\ Sr2: d>\dfrac{2\pi-3\varphi}{2\pi} \end{cases} \tag{15}$$

So, the general ZVS condition is

$$\begin{cases} \dfrac{2\pi-3\varphi}{2\pi}\le d\le\dfrac{-\frac{3n}{D}+\frac{9D(1-D)}{m}\pi+2\pi}{2\pi-3\varphi},\quad \varphi\ge 0\\ \dfrac{\frac{3n}{D}-\frac{9D(1-D)}{m}\pi+2\pi+3\varphi}{2\pi}\le d\le\dfrac{2\pi}{2\pi+3\varphi},\quad \varphi\le 0. \end{cases} \tag{16}$$

In the worst case, when φ is 0

$$1+\frac{\frac{3n}{D}-\frac{9D(1-D)}{m}\pi}{2\pi}\le d\le 1+\frac{-\frac{3n}{D}+\frac{9D(1-D)}{m}\pi}{2\pi}. \tag{17}$$

In (17), it can be seen that if $P_{\rm pv}$ is large enough to make $d<1$, there will always be hard switching when φ is 0. The solution of d exists only when

$$\frac{9D(1-D)}{m}\pi\ge\frac{3n}{D}\rightarrow m\le\frac{3D^2(1-D)\pi}{n}. \tag{18}$$

Based on (18), ZVS can be guaranteed by selecting proper m. According to (16), the ZVS boundaries can be derived and plotted in Fig. 8.

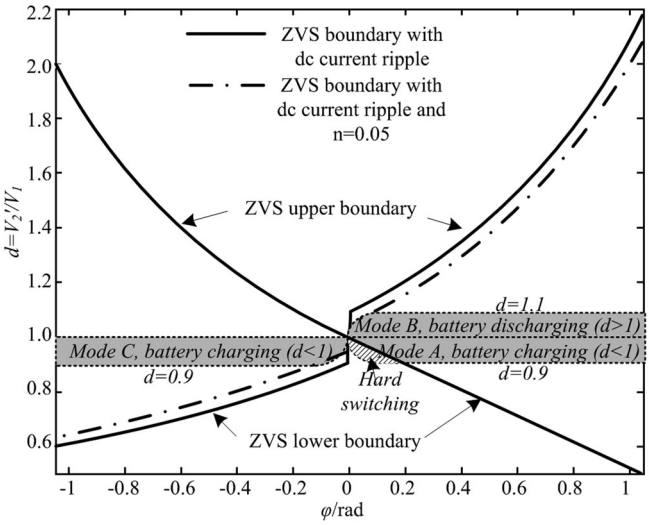

Fig. 8. ZVS in the "three-port" condition including Modes A, B, and C.

In Fig. 8, d is set to the extreme case at discharging and charging modes, and n is selected as 0.1, which is half of the rated power. The operation curves are located between the upper and lower ZVS boundaries except Mode A when the phase-shift angle is small and d is less than 1, but the ZVS range is still improved compared to that of the DAB3 converter.

B. Conduction Loss Analysis

Although integrated multiport converters reduce the number of semiconductor components, many multiport converters induce the circulating current issue to increase the conduction loss [14]–[18]. Since the circulating current may result in extra conduction loss, the conduction loss of the proposed converter is analyzed and compared with that of the conventional two-port three-phase converter presented in [23]. Without loss of generality, the conduction loss of Mode B in the three-port converter is compared with that of the two-port converter. In addition, Mode E of the three-port converter is also selected since it is a two-port operation. The currents of Mode B in transformers and secondary-side switches are the same as those in two-port cases; therefore, the conduction loss of primary-side switches S_{a1} and S_{a2} is studied. The current waveforms of Mode B in S_{a1} and S_{a_2} are calculated in (19) and plotted in Fig. 9(a) where with the same rated output power $P3$, the RMS current in upper switches S_{a1} decreases but the one in lower switch S_{a2} increases. This is different when compared to the two-port case since the current waveforms in primary-side switches of Mode B are not equal due to the PV current. The conduction loss is proportional to $I_{\rm rms}^2$ that is shown in Fig. 9(b). It can be observed that the conduction losses of different modes of the three-port converter are

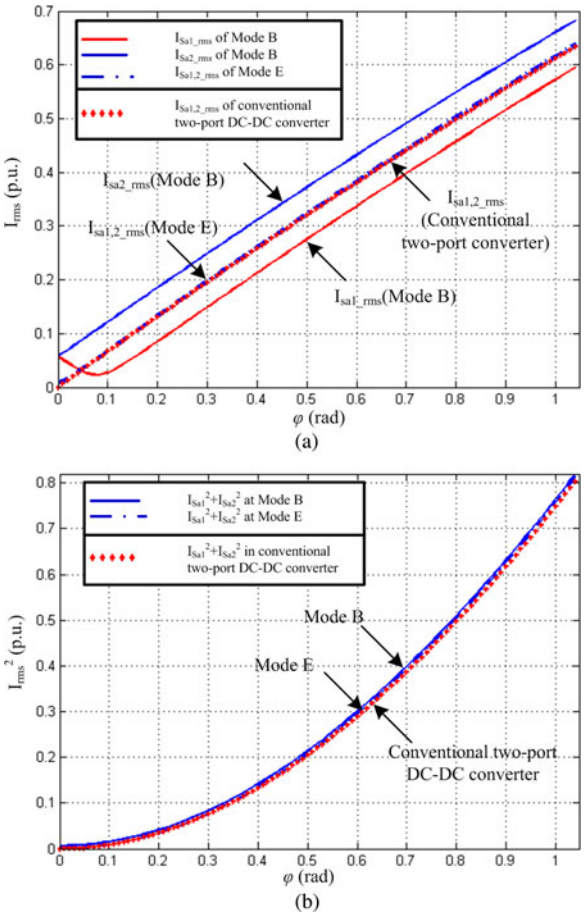

Fig. 9. (a) RMS currents of S_{a1} and S_{a2} in Modes B, E, and the two-port converter. (b) Conduction losses of S_{a1} and S_{a2} in Modes B, E, and the two-port converter ($R_{\mathrm{ds_on}} = 1$p.u).

close to that of the two-port converter. So, the integrated three-port converter proposed in this paper does not suffer conduction loss penalty but, on the other hand, can reduce the number of semiconductor components

$$\begin{cases} I_{\mathrm{rms\_}Sa1} = \sqrt{\dfrac{1}{2\pi} * \displaystyle\int_0^{2D\pi} (i_{sa}(\theta) - i_{\mathrm{DC}a}(\theta))^2 d\theta} \\ I_{\mathrm{rms\_}Sa2} = \sqrt{\dfrac{1}{2\pi} * \displaystyle\int_{2D\pi}^{2\pi} (i_{\mathrm{DC}a}(\theta) - i_{sa}(\theta))^2 d\theta}. \end{cases} \tag{19}$$

IV. Control System Design

The power between the primary side and secondary side in Area III $(1/3 < D < 2/3, \varphi < 2\pi(D - 1/3), \varphi < 2\pi(2/3 - D))$ is

$$P_3 = \frac{V_d V_o'}{\omega L_s} \frac{\varphi(4\pi - 3|\varphi|)}{6\pi}. \tag{20}$$

Different from the single-phase DHB converter [25] and DAB converter [16], the power is only related to the phase-shift angle φ but does not depend on D. The three-port converter can be treated as a three-phase boost converter with duty cycle control connected to a three-phase DAB converter with phase-shift angle control, which is shown in Fig. 10. It becomes a conventional two stage dc–dc converter, and the controller includes the boost controller and DAB controller with fixed duty cycle. Fig. 11 illustrates the controller for two converters. The MPPT can be realized by controlling the duty cycle D. $G_{id\_\mathrm{boost}}(s)$ is the duty cycle to current transfer function of the boost converter. The output current i_3 on the HVS is controlled by the current controller $C_i(s)$ of the DAB3 converter, and $G_{i\varphi\_\mathrm{DAB}}(s)$ is the phase shift to current transfer function of the DAB3 converter. The reference of i_3 is varied in different scenarios. When the battery SOC controller is activated for battery power management, the reference is determined by the battery's reference current, i.e., $i_{3a}^* = (P_{\mathrm{PV}} - P_{\mathrm{Bat}}^*)/V_3$. Otherwise, the reference is i_{3b}^* given by the load requirement from the high-voltage dc bus.

For the three-phase DAB converter, since there are 12 subperiods in one switching cycle, it is much more complicated to derive the full-order small-signal model than that in a full-bridge DAB converter [26], [27]. According to the power (20), the average state equation can be written as

$$\begin{cases} C_2 \dfrac{dV_2}{dt} = i_{23} - i_{\mathrm{in\_DAB3}} \\ C_3 \dfrac{dV_3}{dt} = -\dfrac{V_3}{R} - i_{o\_\mathrm{DAB3}} \end{cases} \tag{21}$$

where $i_{\mathrm{in\_DAB3}} = \frac{P_3}{V_2} = \frac{V_3'}{\omega L_s} \frac{\varphi(4\pi - 3|\varphi|)}{6\pi}$, $i_{o\_\mathrm{DAB3}} = \frac{P_3}{V_3'} = \frac{V_2}{\omega L_s} \frac{\varphi(4\pi - 3|\varphi|)}{6\pi}$.

The small-signal model can be derived by expanding the average model into Taylor series around the operating point, and then neglecting the higher order nonlinear terms, which is described as follows:

$$\begin{cases} C_2 \dfrac{d\hat{v}_2}{dt} = -m_1 \hat{\varphi} - g\hat{v}_o \\ C_3 \dfrac{d\hat{v}_3}{dt} = -\dfrac{\hat{v}_3}{R} + m_2 \hat{\varphi} + g\hat{v}_d \end{cases} \tag{22}$$

where $m_1 = \frac{V_3'(4\pi - 6|\varphi|)}{6\pi\omega L_s}$, $m_2 = \frac{V_2(4\pi - 6|\varphi|)}{6\pi\omega L_s}$, and $g = \frac{\varphi(4\pi - 3|\varphi|)}{6\pi\omega L_s}$.

The output current to control transfer function can be derived as

$$G_{i\varphi}(s) = \frac{1}{R} G_{v\varphi}(s) = \frac{sC_2 m_2 - g m_1}{s^2 C_2 C_3 + s\frac{C_2}{R} + g^2}. \tag{23}$$

A controller is designed based on a converter prototype built in the laboratory. The converter's parameters are listed in Table II. The duty cycle D is controlled by the MPPT controller, and the phase-shift angle control is implemented by the compensator $C_i(s)$, which is expressed as

$$C_i(s) = \frac{K_i\left(\frac{s}{\omega_z} + 1\right)}{s\left(\frac{s}{\omega_p} + 1\right)} \tag{24}$$

where $K_i = 1200$, $\omega_z = 6280$ rad/s, and $\omega_p = 62\,800$ rad/s.

After compensation, the cross frequency of the current open loop is 1.69 kHz and the phase margin is 56°, which is shown in Fig. 12.

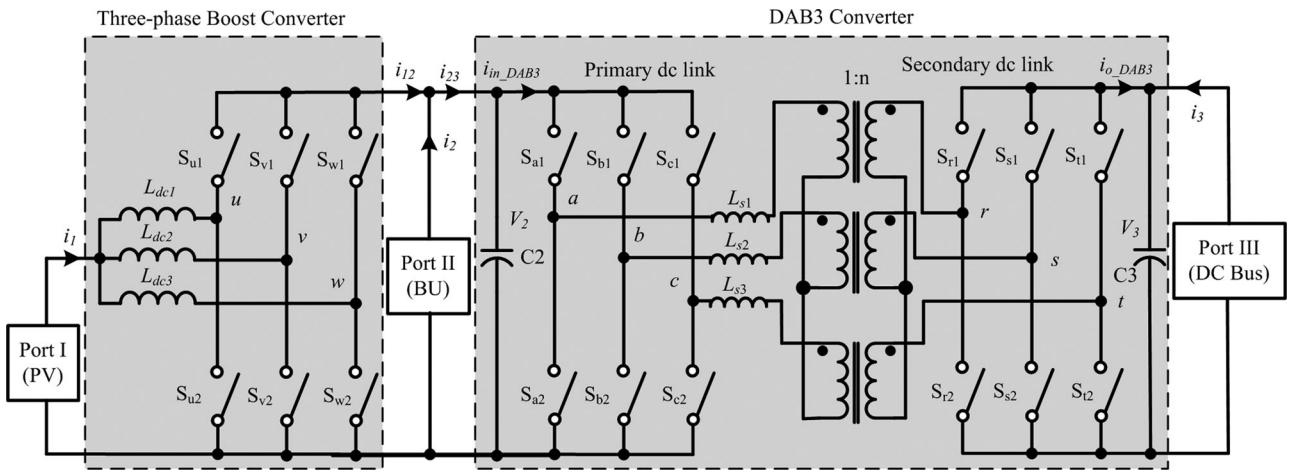

Fig. 10. Equivalent circuit of the three-port dc–dc converter.

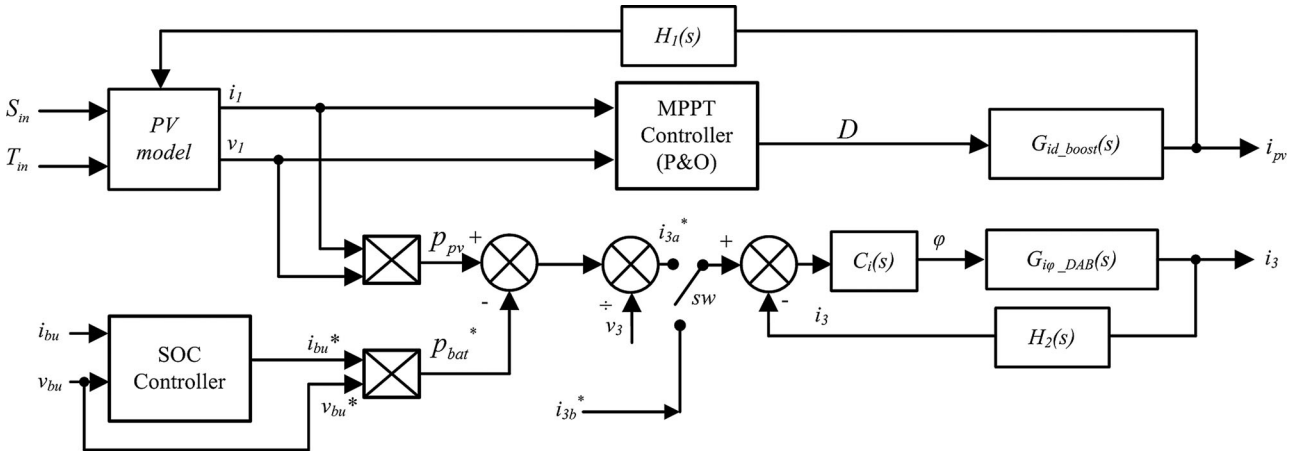

Fig. 11. Control system diagram.

TABLE II
CONVERTER PARAMETERS

DC bus voltage V_3	270V
Battery voltage V_2	67.5V
PV voltage V_1	32~48V
Rated power P_3	3kW
Switching frequency f	40kHz
Transformer turns ratio	1:4
Leakage inductor L_s	1μH
DC inductor L_{dc}	7.5μH
Input capacitor C_2	5600μF
DC-link capacitor C_3	780 μF

The average model of the three-port dc–dc converter is developed for verification of operation mode simulation. Based on the equivalent circuit, the converter can be divided into two stages: boost stage and DAB3 stage. According to (20), the average model can be derived, which is shown in Fig. 13.

The comparison of the three-port converter, the equivalent circuit, and the average model is simulated and displayed in Fig. 14, in which the load power changes from 4150 to 6150 W at 0.2 s and changes back to 4150 W at 0.25 s, and the PV voltage changes from 32 to 42 V with a finite slope. In the equivalent circuit, the duty cycle D of the DAB3 stage is fixed at 0.5.

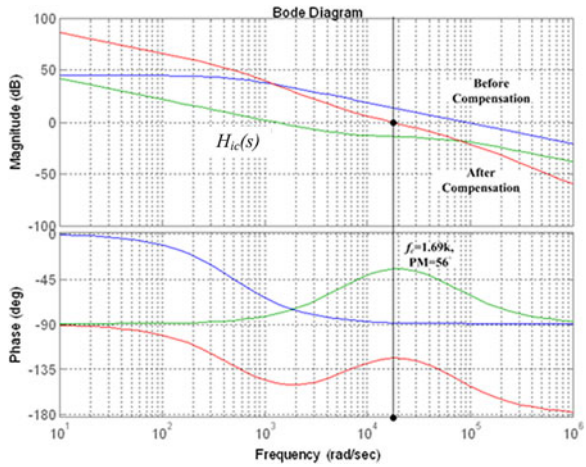

Fig. 12. Current open-loop gain of the DAB3 stage built in the laboratory.

The simulation results show that the three models are almost consistent with each other. The difference happens when the output current is high and the input voltage is relatively large. In this condition, the converter is operating in Area V which has

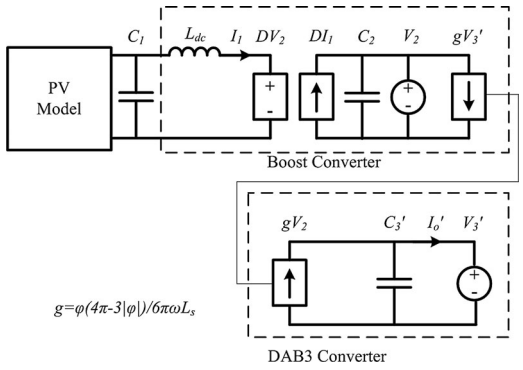

Fig. 13. Average model of the three-port dc–dc converter.

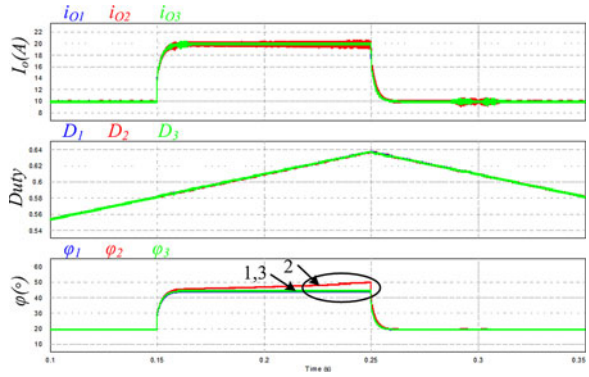

Fig. 14. Simulation results comparison: 1—circuit model; 2—equivalent circuit model; 3—average model.

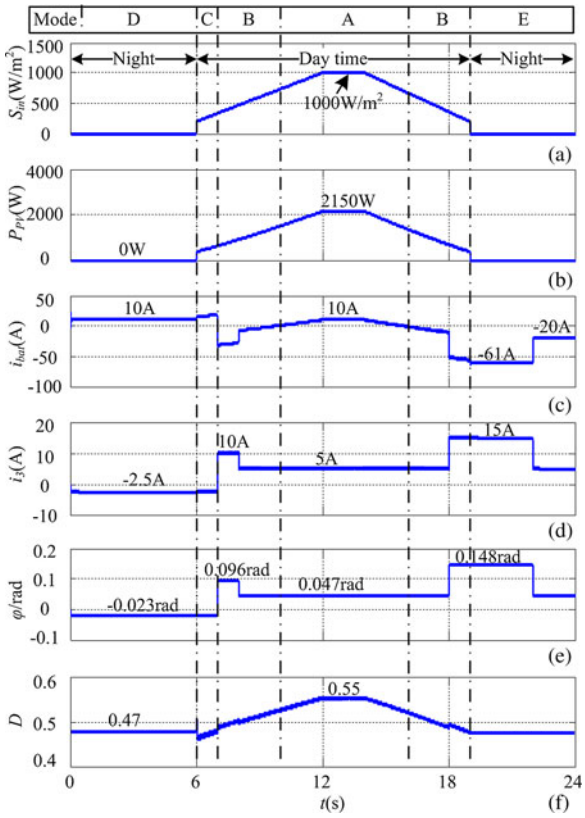

Fig. 15. One-day simulation results using the average model.

different power equations [24], i.e.,

$$P_V = \frac{V_2 V_3'}{\omega L_s}\left(\frac{\varphi(4\pi - 3|\varphi|)}{6\pi} - \frac{[2\pi(2-3D) - 3|\varphi|]^2}{36\pi}\right). \tag{25}$$

Under this condition, the controlled phase-shift angle is not consistent with each other. Considering that the difference of power equation in Areas III and V is no more than 10%, the average model derived from Area III can still be applied approximately in the whole operation range.

Fig. 15 shows the one-day scaled down simulation results of the proposed controller based on the average model. In Fig. 15, from 0 to 6 s, there is no solar power, and the dc distribution bus provides power to charge the battery, so the converter is operating in Mode D. At 6 s, solar irradiation starts to increase from 200 to 1000 W/m^2. From 6 to 7 s, the PV together with the dc distribution bus generates power to charge the battery, and the converter is operating in Mode C. At 7 s, there is a peak power requirement on the dc distribution bus side, and PV and the battery provide power to the dc-bus load. The converter operates in Mode B when the PV power is lower than the dc-bus load requirement, and operates in Mode A when the PV power is higher than the dc-bus load. At 18 s, there is another peak power requirement from the dc-bus side, and the battery provides main power due to the low solar irradiation level. After 19 s, the solar power is zero, and the dc-bus load is supported by the battery, so the converter is operating in Mode E. From Fig. 15, it can be seen that when the irradiation changes, only duty cycle is controlled to realize the MPPT. Phase-shift angle only changes when there is power flow response between the two sides such as variation of battery's charging current or dc load current.

V. Experimental Verifications

A three-port bidirectional PV system is developed in the laboratory, which is shown in Fig. 16. Forty-kHz high-frequency transformers are designed for a 3-kW three-phase bidirectional dc–dc converter. A digital controller is applied to achieve the control algorithm. The duty cycle varies between 1/3 and 2/3 according to different PV voltages. Although the phase-shift angle φ can change from $-2\pi/3$ to $2\pi/3$, it is limited between $-\pi/6$ and $\pi/6$ to maintain the high efficiency. The conduction loss of the converter will not change too much when the duty cycle changes from 1/3 to 2/3, because the RMS current in the converter almost keeps constant [24]. The PV array is emulated by a 4-kW PV emulator and connected to the primary-side current-fed port of the converter. The parameters of the PV array are $V_{\rm pm} = 40$ V, $V_{\rm oc} = 48$ V, $I_{\rm mp} = 5 \times 5.4$ A, and $I_{\rm sc} = 5 \times 5.8$ A. Five U27-12RT 12.8 V lithium iron magnesium phosphate battery modules connected in series are employed as an energy storage element [28]. The batteries' voltage drops to $12.9 \times 5 = 64.5$ V at 60% SOC and the maximum discharging current rating is 30 A (0.2 C). The batteries' voltage increases

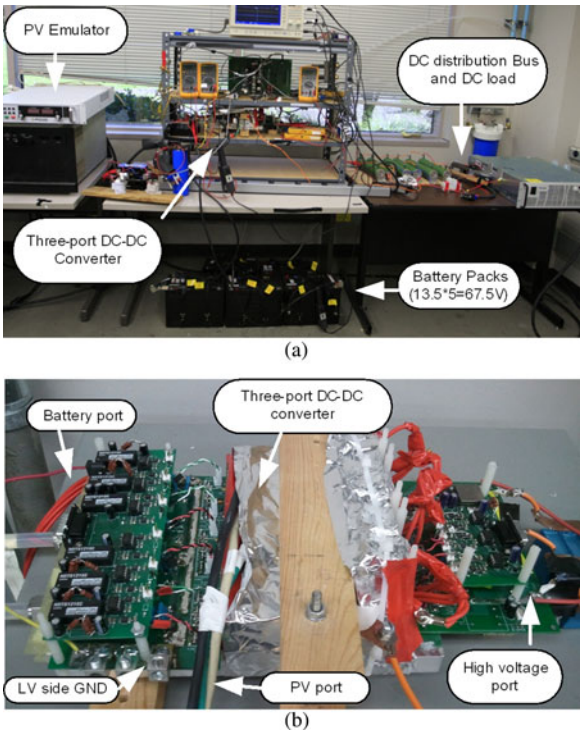

Fig. 16. (a) Developed PV system test bed and (b) the three-port three-phase bidirectional dc–dc converter.

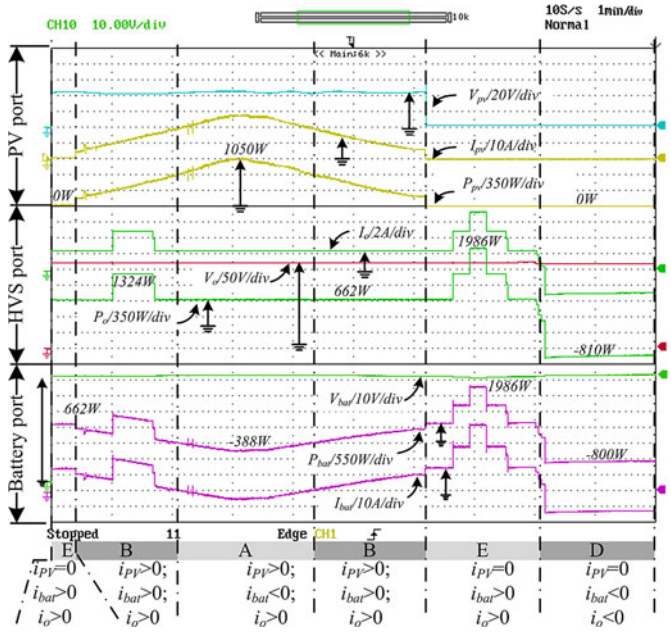

Fig. 17. One-day experimental results with the solar irradiation and load variation.

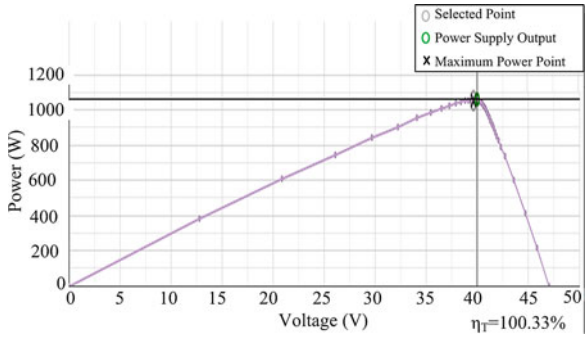

Fig. 18. PV emulator generates maximum power by MPPT control at solar irradiation 950 W/m^2.

to $14.5 \times 5 = 72.5$ V at 100% SOC and the maximum charging current is 15 A (0.1 C). The secondary-side dc link of the converter is connected to a 270-V dc distribution bus. Therefore, d is between 0.93 and 1.05. The dc inductor is 7.5 μH, and the leakage inductance is 1 μH. So, m is 7.5 and the value of n is 0.06 when PV generates maximum power.

Fig. 17 shows the experimental voltage and current waveforms of three ports during one day with the load and irradiation change. In the morning, before the sunrise, the load power is provided by the battery, and the converter is operated in Mode E. When the irradiation increases from 0, the PV panels begin to provide power, and the converter is operated in Mode B. With the irradiation increasing, the PV power increases and surpasses the load requirement, and the excessive power is stored in the battery. In this case, the converter is operated in Mode A. The solar irradiation increases from 150 W/m^{2}to the maximum value 950 W/m^{2}and then begins to decrease in the afternoon. As shown in Fig. 18, the PV emulator can achieve the maximum power by a duty cycle-based P&O MPPT controller. After sunset, the PV panels stop to provide power but only battery supports the load, and the converter is in Mode E. During one day, there are two load peaks that happen in the morning and evening, respectively. The dc distribution bus can be supported by the utility through the ac–dc converter, so during the midnight, the utility power is used to charge the battery due to the low electricity price. The converter is operated in Mode D. The experimental results are consistent with the simulation results to demonstrate that the MPPT can be realized by duty cycle control, and it is independent with the phase-shift control that is used to control the power flow between the primary side and secondary side. Therefore, flexible power management control can achieve different operation modes by the proposed converter which is verified in the experiment.

The experimental results also verified that the switches of the proposed converter can achieve ZVS in different operation modes. Fig. 19(a)–(e) shows the voltage waveforms on the lower switch S_{a2} in different operation modes, since the lower switches on the primary side are the hardest to realize ZVS conditions. Although the battery's voltage will change according to different SOCs and charging/discharging status, the soft switching can still be guaranteed with the help of dc inductor's current ripple. It can be seen that S_{a2} is operating in soft-switching conditions in different operation modes. The ZVS waveforms of the secondary side switch S_{r2} in Mode D are selected as an example [see Fig. 19(f)] to demonstrate that there is larger

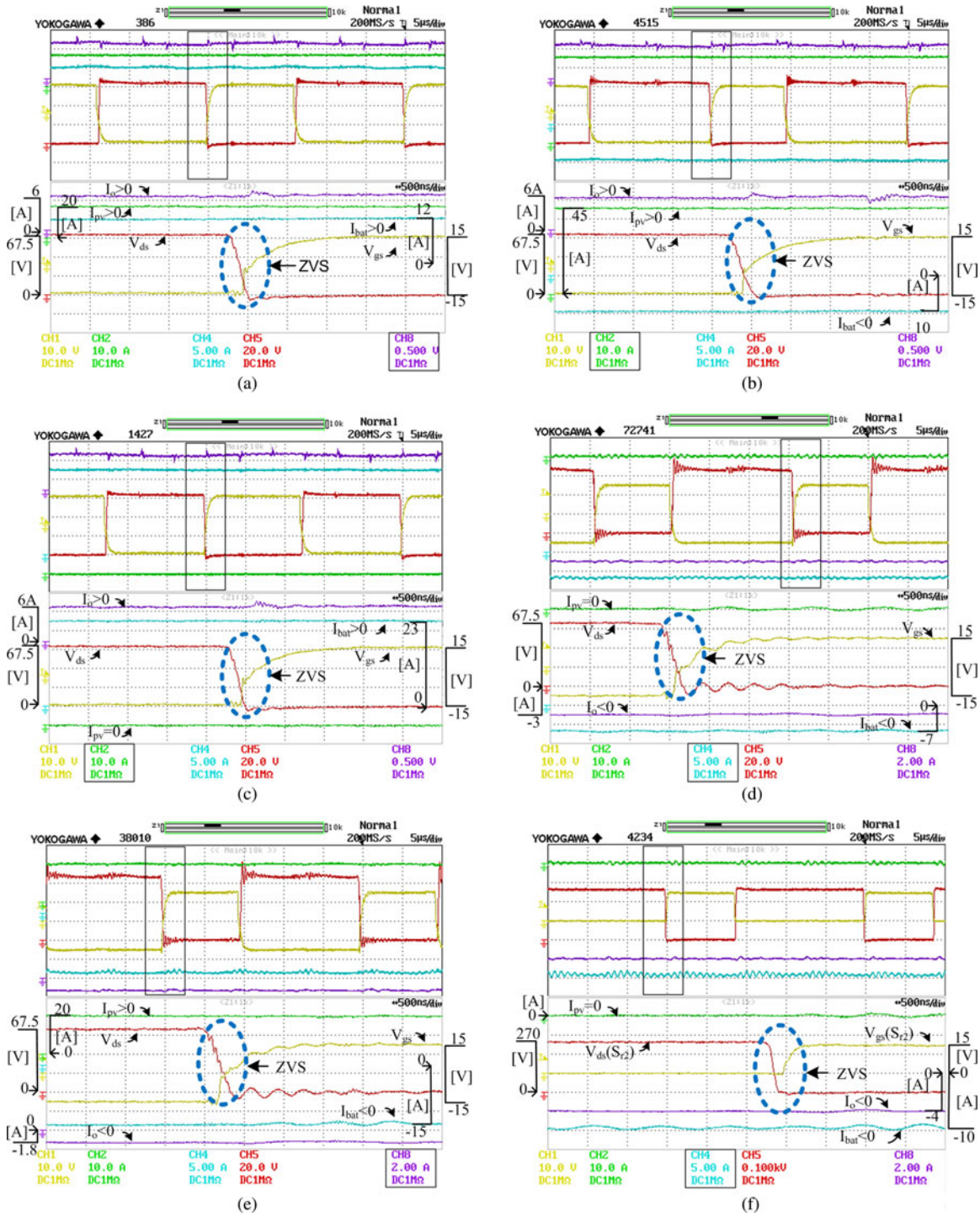

Fig. 19. ZVS waveforms of (a) Sa2 in Mode A; (b) Sa2 in Mode B; (c) Sa2 in Mode C; (d) Sa2 in Mode D; (e) Sa2 in Mode E; and (f) S_{r2} in Mode D.

soft-switching margin for the secondary-side switch than that for the primary-side switches.

VI. Conclusion

In this paper, a PV system with battery as an energy storage element using a three-port three-phase interleaved bidirectional dc–dc converter was proposed for a dc distribution bus application. The high-frequency transformers provide voltage boost capability and galvanic isolation. PV panels and battery interfacing with different types of ports can realize MPPT and soft switching under wide variation of PV voltage. It is also proved that in the three-phase system, the two control variables, duty cycle D and phase-shift angle φ, can be controlled independently to realize MPPT and power flow between energy sources and load without coupling penalty. The benefit of bidirectional power flow is helpful to realize the battery SOC management. In addition, the theoretical analysis is derived to show that with

the help of dc inductors' current ripples, soft-switching conditions can be guaranteed in different operation modes even though the battery's voltage changes due to different SOCs and charging/discharging status. Finally, both simulation and experimental results verified the advantages of the proposed converter.

APPENDIX
DERIVATIONS OF ZVS CONDITIONS

In the general case, the ZVS conditions of each switch is rewritten as

$$\begin{cases} Sa1 : i_{\rm dc}(t_{Sa1\_on}) - i_{Ls}\left(t_{Sa1\_on}\right) > 0 \\ Sa2 : -i_{\rm dc}(t_{Sa2\_on}) + i_{Ls}\left(t_{Sa2\_on}\right) > 0 \\ Sr1 : i_{Ls}\left(t_{Sr1\_on}\right) > 0 \\ Sr2 : i_{Ls}\left(t_{Sr2\_on}\right) < 0 \end{cases} \tag{A1}$$

where the dc inductor current $i_{\rm dc}(t)$ changes with time

$$\begin{cases} i_{\rm dc}\left(t_{Sa1\_on}\right) = i_{\rm dc\_avg} + \dfrac{1}{2}\Delta I_{\rm dc} \\ i_{\rm dc}\left(t_{Sa2\_on}\right) = i_{\rm dc\_avg} - \dfrac{1}{2}\Delta I_{\rm dc} \end{cases} \tag{A2}$$

and the transformer current $i_{Ls}(t)$ will change with different operation areas. Since in the steady state, the average transformer current is zero and voltage–second balance should be satisfied, the transformer current $i_{Ls}(t)$ at time t_{Sa1_on} can be calculated as

$$i_{Ls}\left(t_{Sa1\_on}\right) = \begin{cases} -\dfrac{V_d}{\omega L_s}\dfrac{2d\pi - 2\pi + 3d\varphi}{9}, & \text{Area II} \\ -\dfrac{V_d}{\omega L_s}\dfrac{2d\pi - 2\pi - 3\varphi}{9}, & \text{Area III} \\ \dfrac{V_d}{\omega L_s}\dfrac{2\left[3d(1-D)\pi - \pi - 3d\varphi\right]}{9}, \quad \varphi \geq 0 & \text{Area V.} \end{cases} \tag{A3}$$

The transfer current at the other time can be calculated in the same way. When φ is negative, $i_{Ls}\left(t_{Sa1_{\rm on}}\right)$ and $i_{Ls}\left(t_{Sr1_{\rm on}}\right)$ are exchanged. The dc inductor current ripple is

$$\Delta i_{\rm DC} = \frac{V_d - DV_d}{\omega L_{\rm dc}} 2D\pi = \frac{V_d}{\omega L_s}\frac{2D(1-D)\pi}{m} \tag{A4}$$

where $m = {L_{\rm dc}}/{L_s}$.

The average dc inductor current can be calculated by

$$i_{\rm dc\_avg} = \frac{P_{\rm PV}}{3V_{\rm PV}} = \frac{nV_d^2}{3\omega L_s D V_d} = \frac{V_d}{\omega L_s}\frac{n}{3D}. \tag{A5}$$

The rated power of the converter at φ_0 is

$$P_0 = \frac{V_d^2}{\omega L_s}\frac{\varphi_0\left(4\pi - 3\left|\varphi_0\right|\right)}{6\pi}. \tag{A6}$$

In order to maintain the high efficiency and lower reactive power, φ_0 should not be high. If φ_0 is selected as $\pi/9$, the rated power P_0 is

$$P_0 \approx 0.2\frac{V_d^2}{\omega L_s}. \tag{A7}$$

The PV power should be less than P_0, i.e., $n < 0.2$.

TABLE III
ZVS CONDITIONS IN DIFFERENT OPERATION AREAS

Operation Area		ZVS Conditions	ZVS Condition at $\varphi = 0$
II	$\varphi \geq 0$	$max\left\{3D - \frac{3\varphi}{\pi}, 1 - \frac{3\varphi}{2\pi}\right\} \leq d \leq min\left\{\frac{2\pi + k_1 - k_2}{6(D\pi - \varphi)}, \frac{2\pi + k_1 - k_2}{(2\pi - 3\varphi)}\right\}$	$1 \leq d \leq 1 + \frac{k_1 - k_2}{2\pi}$
	$\varphi \leq 0$	$max\left\{3D + \frac{3\varphi + k_2 - k_1}{\pi}, 1 + \frac{3\varphi + k_2 - k_1}{2\pi}\right\} \leq d \leq min\left\{\frac{2\pi}{2\pi + 3\varphi}, \frac{\pi}{3D\pi + 3\varphi}\right\}$	$1 - \frac{k_1 - k_2}{2\pi} \leq d \leq 1$
III	$\varphi \geq 0$	$\frac{2\pi - 3\varphi}{2\pi} \leq d \leq \frac{2\pi + k_1 - k_2}{2\pi - 3\varphi}$	$1 \leq d \leq 1 + \frac{k_1 - k_2}{2\pi}$
	$\varphi \leq 0$	$1 + \frac{3\varphi + k_2 - k_1}{2\pi} \leq d \leq \frac{2\pi}{2\pi + 3\varphi}$	$1 - \frac{k_1 - k_2}{2\pi} \leq d \leq 1$
V	$\varphi \geq 0$	$max\left\{3D' - \frac{3\varphi}{\pi}, 1 - \frac{3\varphi}{2\pi}\right\} \leq d \leq min\left\{\frac{2\pi + k_1 - k_2}{6(D'\pi - \varphi)}, \frac{2\pi + k_1 - k_2}{(2\pi - 3\varphi)}\right\}$	$1 \leq d \leq 1 + \frac{k_1 - k_2}{2\pi}$
	$\varphi \leq 0$	$max\left\{3D' + \frac{3\varphi + k_2 - k_1}{\pi}, 1 + \frac{3\varphi + k_2 - k_1}{2\pi}\right\} \leq d \leq min\left\{\frac{2\pi}{2\pi + 3\varphi}, \frac{\pi}{3D'\pi + 3\varphi}\right\}$	$1 - \frac{k_1 - k_2}{2\pi} \leq d \leq 1$

Where $k_1 = \frac{9DD'}{m}\pi, k_2 = \frac{3|n|}{D}, D' = 1 - D$.

Substituting (A2)–(A5) into (A1), the ZVS conditions in different cases can be calculated and summarized in Table III where $k_1 = \frac{9DD'}{m}\pi, k_2 = \frac{3|n|}{D}, D' = 1 - D$.

According to Table III, it can be seen that the ZVS range changes with k_1 and k_2. k_1 can help enlarge the ZVS range but k_2 reduces it. If $k_1 > k_2$, the converter can operate with the ZVS at $\varphi = 0$, which can be derived as

$$m < \frac{3D^2D'}{|n|}\pi. \tag{A8}$$

REFERENCES

[1] D. Nilsson and A. Sannino, "Efficiency analysis of low- and medium-voltage DC distribution systems," in *Proc. IEEE Power Eng. Soc. Gen. Meet.*, Jun. 6–10, 2004, vol. 2, pp. 2315–2321.

[2] W. Kramer, S. Chakraborty, B. Kroposki, and H. Thomas, "Advanced power electronic interfaces for distributed energy systems—I: System and topologies," National Renewable Energy Laboratory, Golden, CO, Tech. Rep. NREL/TP-581–42672, Mar. 2008.

[3] K. Kurohane, A. Uehara, T. Senjyu, A. Yona, N. Urasaki, T. Funabashi, and C. Kim, "Control strategy for a distributed DC power system with renewable energy," *Renewable Energy*, vol. 36, no. 1, pp. 42–49, Jan. 2011.

[4] G. Byeon, H. Lee, T. Yoon, G. Jang, W. Chae, and J. Kim, "A research on the characteristics of fault current of DC distribution system and AC distribution system," in *Proc. IEEE 8th Int. Conf. Power Electron. ECCE Asia*, May 30–Jun. 3, 2011, pp. 543–550.

[5] M. Brenna, E. Tironi, and G. Ubezio, "Proposal of a local DC distribution network with distributed energy resources," in *Proc. 11th Int. Conf. Harmonics Quality Power*, Sep. 12–15, 2004, pp. 397–402.

[6] S. Kai, Z. Li, X. Yan, and J. M. Guerrero, "A distributed control strategy based on DC bus signaling for modular photovoltaic generation systems with battery energy storage," *IEEE Trans. Power Electron.*, vol. 26, no. 10, pp. 3032–3045, Oct. 2011.

[7] M. Bash, R. R. Chan, J. Crider, C. Harianto, J. Lian, J. Neely, S. D. Pekarek, S. D. Sudhoff, and N. Vaks, "A medium voltage DC testbed for ship power system research," in *Proc. IEEE Electr. Ship Technol. Symp.*, Apr. 20–22, 2009, pp. 560–567.

[8] G.-S. Seo, J. Baek, K. Choi, H. Bae, and B. Cho, "Modeling and analysis of DC distribution systems," in *Proc. IEEE 8th Int. Conf. Power Electron. ECCE Asia*, May 30–Jun. 3, 2011, pp. 223–227.

[9] D. Lu, H. Fakham, T. Zhou, and B. Francois, "Application of Petri nets for the energy management of a photovoltaic based power station including storage units," *Renewable Energy*, vol. 35, pp. 1117–1124, 2010.

[10] Y. Riffonneau, S. Bacha, F. Barruel, and S. Ploix, "Optimal power flow management for grid connected PV systems with batteries," *IEEE Trans. Sustainable Energy*, vol. 2, no. 3, pp. 309–320, Jul. 2011.

[11] P. Denholm and R. M. Margolis, "Evaluating the limits of solar photovoltaics (PV) in electric power systems utilizing energy storage and other enabling technologies," *Energy Policy*, vol. 35, no. 9, pp. 4424–4433, Sep. 2007.

[12] Z. Qian, O. Abdel-Rahman, H. Al-Atrash, and I. Batarseh, "Modeling and control of three-port DC/DC converter interface for satellite applications," *IEEE Trans. Power Electron.*, vol. 25, no. 3, pp. 637–649, Mar. 2010.

[13] H. Al-Atrash, F. Tian, and I. Batarseh, "Tri-modal half-bridge converter topology for three-port interface," *IEEE Trans. Power Electron.*, vol. 22, no. 1, pp. 341–345, Jan. 2007.

[14] H. Li and D. Liu, "Power distribution strategy of fuel cell vehicle system with hybrid energy storage elements using triple half bridge (THB) bidirectional DC-DC converter," in *Proc. IEEE 42nd Ind. Appl. Soc. Annu. Meet. Conf. Rec. Ind. Appl. Conf.*, Sep. 23–27, 2007, pp. 636–642.

[15] H. Tao, J. L. Duarte, and M. A. M. Hendrix, "Three-port triple-half-bridge bidirectional converter with zero-voltage switching," *IEEE Trans. Power Electron.*, vol. 23, no. 2, pp. 782–792, Mar. 2008.

[16] H. Tao, A Kotsopoulos, J. L. Duarte, and M. A. M. Hendrix, "Transformer-coupled multiport ZVS bidirectional DC–DC converter with wide input range," *IEEE Trans. Power Electron.*, vol. 23, no. 2, pp. 771–781, Mar. 2008.

[17] C. Zhao, S. D. Round, and J. W. Kolar, "An isolated three-port bidirectional DC-DC converter with decoupled power flow management," *IEEE Trans. Power Electron.*, vol. 23, no. 5, pp. 2443–2453, Sep. 2008.

[18] H. Krishnaswami and N. Mohan, "Three-port series-resonant DC–DC converter to interface renewable energy sources with bidirectional load and energy storage ports," *IEEE Trans. Power Electron.*, vol. 24, no. 10, pp. 2289–2297, Oct. 2009.

[19] L. Wang, Z. Wang, and H. Li, "Asymmetrical duty cycle control and decoupled power flow design of a three-port bidirectional DC-DC converter for fuel cell vehicle application," *IEEE Trans. Power Electron.*, vol. 27, no. 2, pp. 891–904, Feb. 2012.

[20] L. Tang and G.-J. Su, "An interleaved reduced-component-count multivoltage bus DC/DC converter for fuel cell powered electric vehicle applications," *IEEE Trans. Ind. Appl.*, vol. 44, no. 5, pp. 1638–1644, Sep.–Oct. 2008.

[21] G.-J. Su and L. Tang, "A reduced-part, triple-voltage DC–DC converter for EV/HEV power management," *IEEE Trans. Power Electron.*, vol. 24, no. 10, pp. 2406–2410, Oct. 2009.

[22] G.-J. Su and L. Tang, "A multiphase, modular, bidirectional, triple-voltage DC–DC converter for hybrid and fuel cell vehicle power systems," *IEEE Trans. Power Electron.*, vol. 23, no. 6, pp. 3035–3046, Nov. 2008.

[23] R. W. A. A. De Doncker, D. M. Divan, and M. H. Kheraluwala, "A three-phase soft-switched high-power-density DC/DC converter for high-power applications," *IEEE Trans. Ind. Appl.*, vol. 27, no. 1, pp. 63–73, Jan.–Feb. 1991.

[24] Z. Wang and H. Lui, "A soft switching three-phase current-fed bidirectional DC-DC converter with high efficiency over a wide input voltage range," *IEEE Trans. Power Electron.*, vol. 27, no. 2, pp. 669–684, Feb. 2012.

[25] Z. Wang and H. Lui, "Optimized operating mode of current-fed dual half bridges dc-dc converters for energy storage applications," in *Proc. IEEE Energy Convers. Congr. Expo.*, Sep. 20—24 2009, pp. 731–737.

[26] C. Zhao, S. D. Round, and J. W. Kolar, "Full-order averaging modelling of zero-voltage-switching phase-shift bidirectional DC-DC converters," *IET Power Electron.*, vol. 3, no. 3, pp. 400–410, May 2010.

[27] F. Krismer and J. W. Kolar, "Accurate small-signal model for the digital control of an automotive bidirectional dual active bridge," *IEEE Trans. Power Electron.*, vol. 24, no. 12, pp. 2756–2768, Dec. 2009.

[28] U-Charge RT Datasheet (Mar. 2009). [Online]. Available: http://www.valence.com

Authors' photographs and biographies not available at the time of publication.